

Fast two-qubit logic with holes in germanium

<https://doi.org/10.1038/s41586-019-1919-3>

Received: 17 June 2019

Accepted: 8 October 2019

Published online: 13 January 2020

N. W. Hendrickx^{1,2,4}, D. P. Franke^{1,2,4}, A. Sammak^{1,3}, G. Scappucci^{1,2} & M. Veldhorst^{1,2*}

Universal quantum information processing requires the execution of single-qubit and two-qubit logic. Across all qubit realizations¹, spin qubits in quantum dots have great promise to become the central building block for quantum computation². Excellent quantum dot control can be achieved in gallium arsenide^{3–5}, and high-fidelity qubit rotations and two-qubit logic have been demonstrated in silicon^{6–9}, but universal quantum logic implemented with local control has yet to be demonstrated. Here we make this step by combining all of these desirable aspects using hole quantum dots in germanium. Good control over tunnel coupling and detuning is obtained by exploiting quantum wells with very low disorder, enabling operation at the charge symmetry point for increased qubit performance. Spin–orbit coupling obviates the need for microscopic elements close to each qubit and enables rapid qubit control with driving frequencies exceeding 100 MHz. We demonstrate a fast universal quantum gate set composed of single-qubit gates with a fidelity of 99.3 per cent and a gate time of 20 nanoseconds, and two-qubit logic operations executed within 75 nanoseconds. Planar germanium has thus matured within a year from a material that can host quantum dots to a platform enabling two-qubit logic, positioning itself as an excellent material for use in quantum information applications.

Gate-defined quantum dots were recognized early on as a promising platform for quantum information² and many materials have been investigated as hosts for the quantum dots. Initial research mainly focused on the low-disorder semiconductor gallium arsenide^{10,11}. Steady progress in the control and understanding of this system culminated in the initial demonstration and optimization of spin qubit operations¹² and the realization of rudimentary analogue quantum simulations³. However, the omnipresent hyperfine interactions in group III–V materials seriously deteriorate the spin coherence. Considerable improvements to the coherence times could be achieved by switching to the group IV semiconductor silicon, in particular when defining spin qubits in an isotopically purified host crystal with vanishing concentrations of non-zero nuclear spins¹³. This enabled single-qubit rotations with fidelities beyond 99.9%⁷ and the execution of two-qubit logic gates with fidelities up to 98%^{6,8,9}, underlining the potential of spin qubits for quantum computation. Nevertheless, quantum dots in silicon are often formed at unintended locations, and control over the tunnel coupling determining the strength of two-qubit interactions is limited. Moreover, the absence of a sizable spin–orbit coupling for electrons in silicon requires the inclusion of microscopic components such as on-chip striplines or nanomagnets close to each qubit, which complicates the design of large and dense two-dimensional (2D) structures. Scalability thus remains a challenge for these systems, and a platform that can overcome these limitations would be highly desirable.

Hole states in semiconductors¹⁴ typically exhibit strong spin–orbit coupling (SOC), which has enabled the demonstration of fast single-qubit rotations^{15–17}. Furthermore, whereas valley degeneracy

complicates qubit definition for electrons in silicon, this is absent for holes, and excited states can be well separated in energy. In silicon, unfavourable band alignment prevents strain engineering of low-disorder quantum wells for holes, restricting experiments to metal–oxide–semiconductor structures¹⁸. Research on germanium has mostly focused on self-assembled nanowires¹⁹ and has demonstrated single-shot spin readout²⁰ and coherent spin control¹⁷. However, strained germanium can reach hole mobilities²¹ of $\mu > 10^6 \text{ cm}^2 \text{ V}^{-1} \text{ s}^{-1}$, and undoped germanium quantum wells were recently shown to support the formation of gate-controlled hole quantum dots²². Now, the crucial challenge is the demonstration of coherent control in this platform and the implementation of qubit–qubit gates for scalable quantum information with holes.

Here we make this step and demonstrate single- and two-qubit logic with holes in planar germanium. We fabricate devices on silicon substrates, using standard manufacturing materials. We grow undoped strained germanium quantum wells, measured to have high hole mobilities $\mu > 5 \times 10^5 \text{ cm}^2 \text{ V}^{-1} \text{ s}^{-1}$ and a low effective hole mass^{22,23} $m_h = 0.09m_e$, extrapolated to reach $m_h = 0.05m_e$ at zero density²⁴, with m_e the electron rest mass. This allows us to define quantum dots of comparatively large size, and we find excellent control over the exchange interaction between the two dots. We operate in a multi-hole mode, reducing challenges in tuning and characterization, which is advantageous for scaling. We make use of the spin–orbit interaction for qubit driving and perform single-qubit rotations at frequencies exceeding 100 MHz. This advantage of fast driving becomes further apparent in coherently accessing the Hilbert space of a two-qubit system.

¹QuTech, Delft University of Technology, Delft, The Netherlands. ²Kavli Institute of Nanoscience, Delft University of Technology, Delft, The Netherlands. ³Netherlands Organisation for Applied Scientific Research (TNO), Delft, The Netherlands. ⁴These authors contributed equally: N. W. Hendrickx, D. P. Franke. *e-mail: m.veldhorst@tudelft.nl

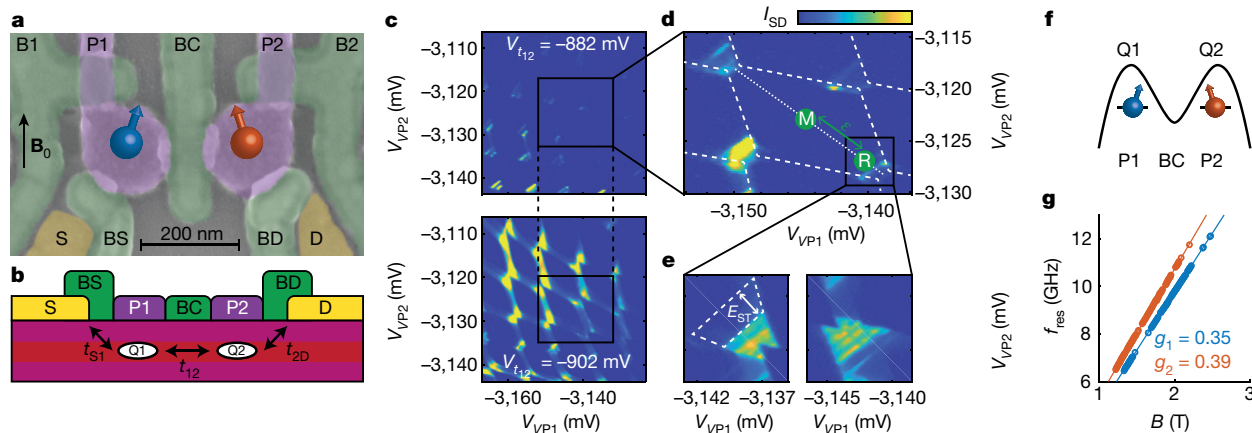


Fig. 1 | Fabrication and operation of a planar germanium double quantum dot. **a**, False-coloured scanning electron microscope image of the two-qubit device, where Ohmic contacts are indicated in yellow, the barrier gate layer is depicted in green and the plunger gate layer in purple. Two hole quantum dots, indicated by the blue and red arrows, are formed in a high-mobility Ge quantum well and controlled by the electric gates. The direction of the external field B_0 is indicated by the black arrow. **b**, Schematic cross-section of the system, where quantum dots are formed below plunger gates P1 and P2, while the different tunnelling rates can be controlled by barrier gates BS, BD and BC. **c**, Transport current through the double dot as a function of plunger gate voltages for weak (top) and strong (bottom) interdot coupling, mediated by a virtual tunnel gate. **d**, Charge stability diagram of the qubit operation point, where the dashed lines

correspond to the charge transitions. The detuning axis ϵ is indicated by the dotted line, with label R corresponding to the qubit readout point. To allow coherent control of the isolated spin states, a two-level voltage pulse on gates P1 and P2 is used to detune the dot potentials and prevent tunnelling to and from the dots during the manipulation phase (label M). **e**, Transport current through the double dot as a function of plunger gate voltage for positive (left) and negative (right) bias. Pauli spin blockade becomes apparent from the suppression of the transport current for the positive bias direction, up to the singlet–triplet energy splitting of $E_{ST} = 0.6$ meV. **f**, Illustration of the energy landscape in our double-quantum dot system. **g**, Resonance frequency, f_{res} , of the two qubits as a function of the external magnetic field, showing the individual qubit resonances.

For example, in silicon the execution of a controlled NOT (CNOT) gate implemented with an on-chip stripline has been shown using microsecond long pulses^{6,8}, and this timescale can be reduced to 0.2–0.5 μ s by incorporating nanomagnets⁹. Here we demonstrate that the spin–orbit coupling of holes in germanium together with the sizable exchange interaction enables a CNOT within 75 ns.

A scanning electron microscope image of the germanium two-qubit device is shown in Fig. 1a. To accumulate holes and define two quantum dots, the circular plunger gates are set to negative potential (V_{P1} , $V_{P2} \approx -2$ V). The tunnel coupling between the dots t_{12} and the tunnel couplings to the source and drain reservoirs (t_{1S} , t_{2D}) are controlled by the barrier gates BC, BS and BD, respectively. Working in a virtual gate voltage space (V_{VP1} , V_{VP2} , V_{t12} , V_{2D} and V_{1D}), we can independently tune these properties (see Supplementary Videos 1–3 online for video-mode operation). We measure the transport current through the double dot system (Fig. 1c, d), and for certain hole occupations (Extended Data Fig. 3) we observe a suppression of the transport current for a positive bias voltage $V_{SD} = 1$ mV, caused by Pauli spin blockade (PSB) (see Fig. 1e). We make use of the blockade as an effective method for spin-to-charge conversion^{2,11}, as well as to initialize our two-qubit system in the blocked $|\downarrow\downarrow\rangle$ ground state.

Taking advantage of the strong spin–orbit coupling¹⁷, we are able to implement a fast manipulation of the qubit states by electric dipole spin resonance (EDSR). We tune the device to a readout point within the PSB region (indicated by the label R in Fig. 1d) and apply an electric microwave excitation to gate P1. When the frequency of the microwave excitation matches the spin resonance frequency of either qubit, PSB is lifted and an increase in the transport current can be observed. We extract the resonance frequency of each qubit as a function of external magnetic field strength B_0 (Extended Data Fig. 4) and observe two distinct qubit resonance lines with g -factors $g_1 = 0.35$ and $g_2 = 0.38$ (Fig. 1g). The difference in g -factors between the two dots is likely to be caused by slightly different hole fillings and thus quantum dot orbitals. As an effect of the spin–orbit coupling, a strong orbital dependence of the effective g -factor is typically measured in hole quantum dots^{18,25}. Furthermore, the effective g -factor can be tuned electrically as a direct

result of the SOC²⁶ (see for example Fig. 3c, d), thereby guaranteeing independent control of the different qubits. We observe that the resonance frequency of both qubits remains stable over several hours, with discrete jumps at longer timescales as presented in Extended Data Fig. 5.

We developed a measurement technique in which we measure the averaged transport current over N repeated pulse cycles and subtract a reference measurement using a lock-in amplifier, to mitigate slow variations in the transport current (see Methods), as is indicated in Fig. 2a. After readout, the system is left in the blocking $|\downarrow\downarrow\rangle$ state, serving as the initialization of our qubits. We now operate the device in the single-qubit transport mode in an external field of $B_0 = 0.5$ T and use the second qubit (Q2) as a readout ancilla. Coherent control over the qubit is demonstrated in a Rabi experiment, where the spin state of qubit 1 (Q1) is measured as a function of microwave pulse length t_p and power P , as shown in Fig. 2b. By increasing the power of the microwave pulse, we can reach Rabi frequencies of over 100 MHz, at an elevated field $B_0 = 1.65$ T (Extended Data Fig. 6).

To determine the control fidelity, which describes the accuracy of our quantum gates, we implement randomized benchmarking of the single-qubit Clifford group²⁷ (Fig. 2c). The measured decay curve of the qubit state as a function of sequence length m is shown in Fig. 2d, from which we extract a single-qubit control fidelity of $F_C = 99.3\%$, using gate times $t_n = 20$ ns and $t_{\pi/2} = 10$ ns. In Fig. 2e, we show the gate fidelities for the different π and $\pi/2$ gates as obtained by interleaved randomized benchmarking, where each randomly drawn gate is followed by the respective interleaved gate (see Fig. 2c). All individual gate fidelities are $F_C > 99\%$, with the infidelity for $\pi/2$ gates being approximately twice as low as for the π gates, on account of the difference in pulse length.

We extensively characterize the coherence in our system at an exchange coupling of $J/h \approx 20$ MHz and find $T_{2,Q1}^* = 833$ ns and $T_{2,Q2}^* = 419$ ns, which can be extended by performing a Hahn echo to $T_{2,Q1}^H = 1.9$ μ s and $T_{2,Q2}^H = 0.8$ μ s (data in Extended Data Fig. 7), as indicated in Fig. 2f. These coherence times compare favourably to $T_2^* = 130$ ns for germanium hut wires¹⁷ and $T_2^* = 270$ ns for holes in silicon²⁸. Electrons in GaAs have an even shorter dephasing time¹¹, with $T_2^* = 10$ ns. The limited T_2^* in GaAs is due to hyperfine interactions,

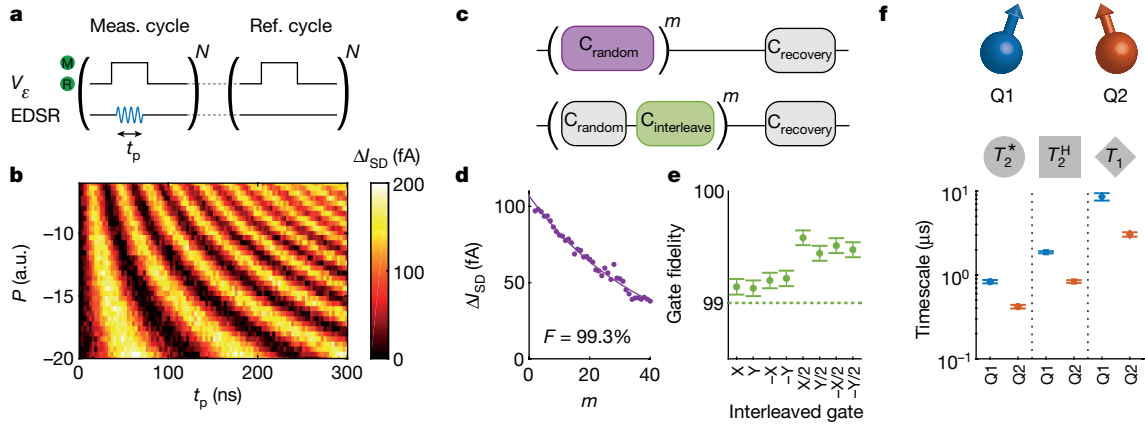


Fig. 2 | Qubit control, gate fidelity and quantum coherence of planar germanium qubits. **a**, Measurement sequence used for the Rabi driving measurements. Measurement cycles with EDSR pulses are alternated with reference cycles without a microwave tone, allowing an efficient background current subtraction. Each cycle is repeated N times, such that measurement and reference cycles alternate at a typical lock-in frequency of $f_{\text{meas}} = 89.75$ Hz. **b**, Colour map of the differential bias current ΔI_{SD} as a function of microwave pulse time t_p and power P , where clear Rabi rotations on Q1 can be

observed. a.u., arbitrary units. **c**, Schematic illustration of the (interleaved) randomized benchmarking sequence applied to Q1. C corresponds to a single Clifford gate, with m being the total number of applied random Clifford gates. **d**, Differential bias current as a function of m for the randomized benchmarking sequence on Q1. The extracted control fidelity is $F_c = (99.3 \pm 0.05)\%$. **e**, Gate fidelities for the π and $\pi/2$ gates. Error bars correspond to 1σ . **f**, Spin coherence and life times for Q1 and Q2. Error bars correspond to 1σ .

which can be mitigated to a large extent by using nuclear notch filtering²⁹, leading to $T_2 = 800$ μs . This source of dephasing can be avoided altogether by using group IV materials with nuclear spin-free isotopes³⁰. This has led to $T_2 = 28$ ms for electrons in isotopically purified silicon¹³, and isotopic purification may also increase the quantum coherence in germanium. Furthermore, we observe spin lifetimes of $T_{1,\text{Q1}} = 9$ μs and $T_{1,\text{Q2}} = 3$ μs . We have found that these lifetimes increase exponentially when lowering the tunnel coupling between each qubit and its respective reservoir (Extended Data Fig. 8), and relaxation times of $T_1 > 100$ μs

have been reported for germanium nanowires^{19,20}, both giving good prospects for increasing the relaxation time by closing the reservoir barrier during operation.

When the manipulation of both qubits is combined, the coupling of the two qubits (exchange interaction/ J) becomes apparent. As is illustrated in Fig. 3a, the resonance frequency of each of the qubits is shifted when the other qubit is prepared in its $|\uparrow\rangle$ state. The strength of this interaction depends on the inter-dot tunnel coupling t_{12} as well as the detuning ε of the dot potentials. By changing the amplitude of voltage

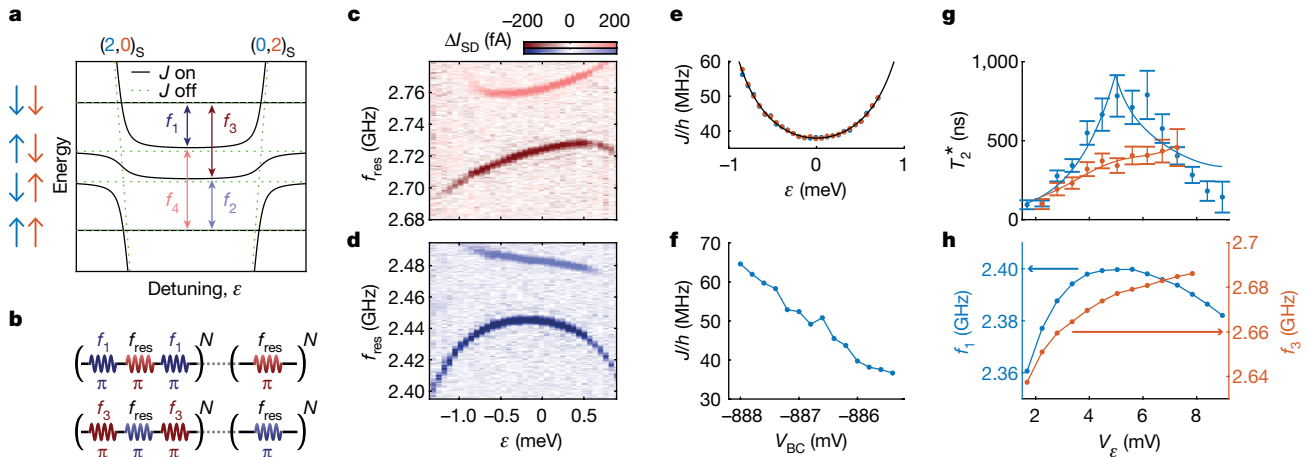


Fig. 3 | Tunable exchange coupling and operation at the charge symmetry point. **a**, Illustration of the relevant energy levels in our hole double quantum dot with zero (green) and finite (black) exchange coupling/ J between the dots. Six energy levels are considered: the four different $(1,1)$ -charge states as well as the $(2,0)_s$ and $(0,2)_s$ singlet charge states in which both holes occupy the same quantum dot. Four individual transitions can be driven, corresponding to the conditional rotations of the two-qubit system. The size of the exchange interaction is equal to $J/h = f_2 - f_1 = f_4 - f_3$. **b**, Measurement pulse cycles used to map out the exchange splitting of Q1 (top) and Q2 (bottom). As a result of the demodulation of the alternating cycles, transition $f_{1,(3)}$ gives a negative signal and transition $f_{2,(4)}$ results in a positive signal. **c**, **d**, EDSR spectra of Q1 (**c**) and Q2 (**d**) as a function of the detuning ε . The exchange splitting can be tuned to a minimum at $\varepsilon = 0$ and increases closer to the $(m, n) - (m + 1, n - 1)$ and $(m, n) - (m - 1, n + 1)$ charge transitions. **e**, Exchange interaction as a function of ε as

extracted from **c**, **d**. Fitting the exchange coupling yields an interdot tunnel coupling $t_{12}/h = 1.8$ GHz and charging energy $U = 1.46$ meV. **f**, The interdot tunnel coupling can also be controlled by gate BC. Changing the potential on this gate, while keeping $\varepsilon = 0$, allows good control over the exchange interaction between the two qubits. **g**, Coherence time T_2^* of both qubits as a function of detuning voltage V_ε . When the slope of the resonance line is equal to zero, the qubit is expected to be, to first order, insensitive to charge noise. Solid lines indicate fits of the data to $\left(a \frac{\partial f_{\text{res}}}{\partial V_\varepsilon} + T_0\right)^{-1}$, with $\frac{\partial f_{\text{res}}}{\partial V_\varepsilon}$ the numerical derivative of the resonance line frequency as a function of detuning, T_0 the residual decoherence and a a scaling factor. It can be observed that T_2^* is indeed longest when the slope of the resonance line is closest to zero. Error bars correspond to 1σ . **h**, Resonance frequency of transition f_1 and f_3 as a function of detuning voltage.

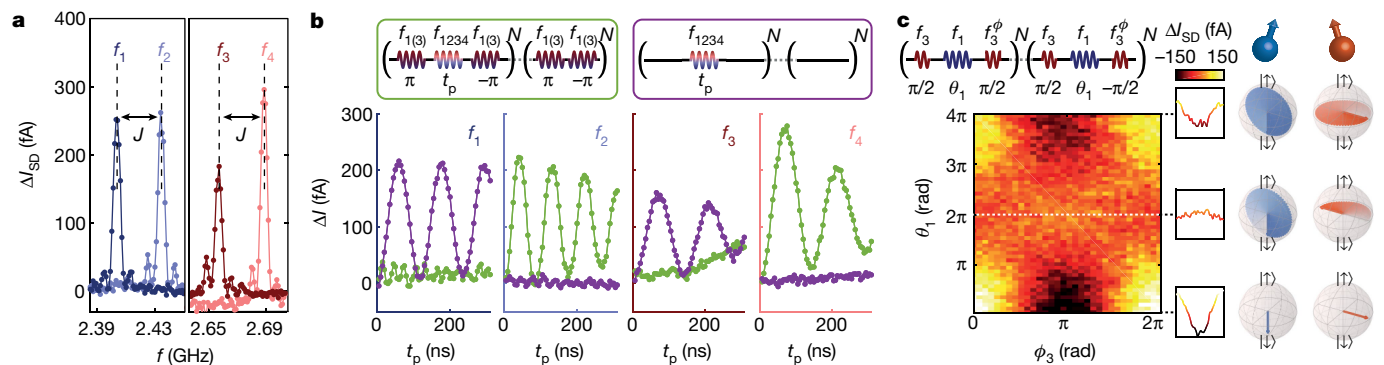


Fig. 4 | Fast two-qubit logic with germanium qubits. **a**, EDSR spectra of both qubits. Resonance peaks can be observed, corresponding to the four individual transitions indicated in Fig. 3a. The peaks are power-broadened, and the linewidth is thus determined by the Rabi frequency. **b**, Controlled qubit rotations can naturally be performed by selectively driving each of the four transitions. A CX gate is achieved at $t_{\text{CX}} = t_r$ on f_1 (f_3). A small off-resonant

driving effect can be observed, which we mitigate by tuning $t_{\text{CX}} = t_{\pi, \text{resonant}} = t_{4\pi, \text{off-resonant}}$. **c**, Colour plot of ΔI_{SD} as a function of Q1 CX-pulse length, θ_1 , and the phase of the second $\pi/2$ -rotation on Q2, ϕ_3 . Owing to the $Z(\theta_1/2)$ rotation on the control qubit, a π phase shift can be observed on Q2 for a conditional 2π rotation on Q1 (f_1).

pulse to point M (dotted line in Fig. 1d), we can map J as a function of the detuning ε . This is shown in Fig. 3c, d, where the subtraction of two pulse sequences in the measurement (see Fig. 3b) results in a positive signal for the unprepared qubit resonances and a negative signal for the prepared states (see Extended Data Fig. 2). As shown in Fig. 3e, the exchange coupling that is reflected in the frequency difference between the initial and prepared resonance positions, is very well described by a simple model^{2,31} using $J = 4Ut_{12}^2/[U^2 - (\alpha\varepsilon - U_0)^2]$. Here, U is the charging energy of the quantum dots, $\alpha = 0.23$ is the lever arm of P1 and P2, and the interdot tunnel coupling is $t_{12}/h = 1.8$ GHz. In addition, the strength of t_{12} can be tuned by using the central barrier BC (Fig. 3f). Here, we use a virtual gate voltage³ V_{r12} , where V_{BC} is set while compensating its influence on the dot potentials by appropriate corrections to V_{p1} and V_{p2} . As a result of this full control over the coupling, we are able to operate the qubits at a mostly charge-insensitive point of symmetric detuning^{4,5}, where the qubit resonance frequencies are the least susceptible to changes in the electric field, while choosing an exchange coupling strength large enough for rapid two-qubit operations. The advantage of this reduced sensitivity to detuning noise is demonstrated in Fig. 3g, where the dephasing time T_2^* of both qubits is measured as a function of ε . Here, T_2^* strongly increases where the slope of $f_{1(3)}$ with respect to the detuning for Q1 (Q2) is minimal, with the longest average phase coherence reached in the flat region at $V_\varepsilon \approx 6$ mV.

The direct control over the tunnel coupling enables us to tune the exchange interaction to a sizable strength of $J/h = 39$ MHz at the symmetry point, as demonstrated in Fig. 4a. We exploit this to obtain fast selective driving and operate in an exchange always-on regime^{8,32}. Full control is obtained by applying microwave pulses at the four resonant frequencies, while further gate pulses controlling J are not needed. A pulse at a single resonance frequency will result in a conditional rotation of the target qubit, as we show in Fig. 4b. A CX-operation can be achieved by setting t_{CX} to give a maximum signal, corresponding to a conditional π -rotation on the target qubit. The slight off-resonant driving that can be observed on f_1 is mitigated by choosing the driving speed such that $t_{\text{CX}} = t_{\pi, \text{resonant}} = t_{4\pi, \text{off-resonant}}$. A fast CX-operation is thus achieved within $t_{\text{CX}, \text{Q1}} = 55$ ns and $t_{\text{CX}, \text{Q2}} = 75$ ns, with Q1 and Q2 as the target qubits respectively.

As a result of the pulsing, we observe a minor shift in the resonance frequency of both qubits, observed before in Si/SiGe quantum dots³³. We compensate the temporary change in resonance frequency by applying phase corrections to all following pulses (see Extended Data Fig. 9). In Fig. 4c, we show the effect of a controlled rotation on the

control qubit with applied phase corrections. We observe a larger signal amplitude on Q1 after 0 and 4π rotations on Q2 as compared with a 2π rotation on Q2. This 4π periodicity is in agreement with fermionic statistics and suggests an echoing pulse correcting residual environmental coupling. The full π phase shift on Q2 for a conditional 2π rotation on Q1, as a result of the $\theta_1/2$ phase that is accumulated by the control qubit, demonstrates the application of a coherent CX gate.

The demonstration of a universal gate set with all-electrical control and without the need of any microscopic structures offers good prospects to scale up spin qubits using holes in strained germanium. The hole states do not suffer from nearby valley states, and the quantum dots are contacted by superconductors²² that may be shaped into microwave resonators for spin–photon coupling. This provides opportunities for a platform that can combine semiconducting, superconducting and topological systems for hybrid technology with fast and coherent control over individual hole spins. Moreover, the demonstrated quantum coherence and level of control make planar germanium a natural candidate to engineer artificial Hamiltonians for quantum simulation, going beyond classically tractable experiments.

Online content

Any methods, additional references, Nature Research reporting summaries, source data, extended data, supplementary information, acknowledgements, peer review information; details of author contributions and competing interests; and statements of data and code availability are available at <https://doi.org/10.1038/s41586-019-1919-3>.

- Ladd, T. D. et al. Quantum computers. *Nature* **464**, 45–53 (2010).
- Loss, D. & DiVincenzo, D. P. Quantum computation with quantum dots. *Phys. Rev. A* **57**, 120–126 (1998).
- Hensgens, T. et al. Quantum simulation of a Fermi–Hubbard model using a semiconductor quantum dot array. *Nature* **548**, 70–73 (2017).
- Reed, M. et al. Reduced sensitivity to charge noise in semiconductor spin qubits via symmetric operation. *Phys. Rev. Lett.* **116**, 110402 (2016).
- Martins, F. et al. Noise suppression using symmetric exchange gates in spin qubits. *Phys. Rev. Lett.* **116**, 116801 (2016).
- Veldhorst, M. et al. A two-qubit logic gate in silicon. *Nature* **526**, 410–414 (2015).
- Yoneda, J. et al. A quantum-dot spin qubit with coherence limited by charge noise and fidelity higher than 99.9%. *Nat. Nanotechnol.* **13**, 102–106 (2017).
- Huang, W. et al. Fidelity benchmarks for two-qubit gates in silicon. *Nature* **569**, 532–536 (2019).
- Zajac, D. M. et al. Resonantly driven CNOT gate for electron spins. *Science* **359**, 439–442 (2018).
- Koppens, F. H. L. et al. Driven coherent oscillations of a single electron spin in a quantum dot. *Nature* **442**, 766–771 (2006).